Electronic Structures and Orbital-Selective Coherence-Incoherence Crossover in $CsFe_2As_2$

Yingjie Shu[1,2], Honglin Zhou[1,2], Jiachen Wang[1,2], Taimin Miao[1,2], Jiuxiang Zhang[1,2], Bo Liang[1,2], Wenpei Zhu[1,2], Neng Cai[1,2], Mingkai Xu[1,2], Yiwen Chen[1,2], Juming Shi[1,2], Shenjin Zhang[3], Fengfeng Zhang[3], Feng Yang[3], Zhimin Wang[3], Qinjun Peng[3], Zuyan Xu[3], Hanqing Mao[1,2], Zhihai Zhu[1,2], Xintong Li[1,2], Guodong Liu[1,2], Huiqian Luo[1,2], Shiliang Li[1,2], Congcong Le[5], Xianxin Wu[4], Lin Zhao[1,2]★ and X. J. Zhou[1,2]★

[1] *Beijing National Laboratory for Condensed Matter Physics, Institute of Physics, Chinese Academy of Sciences, Beijing 100190, China.*

[2] *University of Chinese Academy of Sciences, Beijing 100049, China.*

[3] *Technical Institute of Physics and Chemistry, Chinese Academy of Sciences, Beijing 100190, China.*

[4] *Institute of Theoretical Physics, Chinese Academy of Sciences, Beijing 100190, China.*

[5] *Hefei National Laboratory, Hefei 230088, China*

(Dated: August 21, 2026)

Understanding the role of electron correlations in quasiparticle coherence is central to multiorbital iron-based superconductors. Here, we investigate the electronic structure and temperature-dependent quasiparticle dynamics of $CsFe_2As_2$ using polarization-resolved laser- and synchrotron-based angle-resolved photoemission spectroscopy combined with first-principles calculations. We resolve multiple hole-like Fermi surface sheets around the Γ and M points, with the $\alpha(\alpha')$ and β bands predominantly derived from Fe $3d_{xz/yz}$ orbitals and the γ band mainly from d_{xy}. The calculations reveal a strongly three-dimensional and multiorbital Fermi surface topology, while discrepancies in the detailed orbital character indicate significant correlation effects. Temperature-dependent ARPES further reveals an orbital-selective coherence-incoherence crossover. The α band exhibits a gradual loss of coherence over approximately 50-85 K, accompanied by suppressed spectral weight, increasing linewidth, and evolving dispersion, whereas the β band shows an abrupt collapse of coherent spectral weight near 50-60 K with little change in its dispersion. Together with the resistivity anomaly near 80 K, these results establish a microscopic connection between orbital-selective quasiparticle coherence and macroscopic transport behavior. Our findings provide direct momentum-resolved evidence for band-selective correlation effects in the strongly correlated multiorbital state of $CsFe_2As_2$.

I. INTRODUCTION

Iron-based superconductors provide a unique platform for investigating correlation-driven electronic coherence because their low-energy properties originate from multiple Fe $3d$ orbitals with moderate Coulomb interactions and strong Hund's coupling[1–4]. Since the discovery of superconductivity in iron pnictides, extensive experimental and theoretical studies have revealed that these materials cannot be simply described as weakly correlated metals. Instead, their electronic properties are governed by an intricate interplay among orbital occupancy, Hund's coupling, spin fluctuations, and electronic correlations[1, 2, 5]. In particular, dynamical mean-field theory (DMFT) calculations have suggested that many iron-based superconductors belong to the class of Hund's metals, where Hund's coupling promotes orbital differentiation and strongly suppresses quasiparticle coherence without necessarily

driving the system into a Mott insulating state[6, 7]. Therefore, investigating the evolution from incoherent electronic states to coherent quasiparticles is essential for understanding the electronic ground states of iron-based superconductors.

Among various iron-based superconductors, the heavily hole-doped AFe$_2$As$_2$ (A = K, Rb and Cs) family provides an ideal system for exploring correlation-driven coherence phenomena[8–14]. Compared with the parent compound BaFe$_2$As$_2$, these compounds are located at the extreme hole-doping limit of the 122 phase diagram[9, 15], where electron pockets near the Brillouin-zone corner disappear and the Fermi surface consists exclusively of hole-like bands[16, 17]. The absence of electron-hole compensation and the strongly enhanced effective masses distinguish these materials from other iron pnictides and indicate a distinct electronic regime dominated by strong correlations[9, 11, 13, 15].

CsFe$_2$As$_2$ represents the most strongly correlated member of the AFe$_2$As$_2$ family[12, 13, 15]. Although it exhibits a relatively low superconducting transition temperature ($T_c \approx 2$ K), CsFe$_2$As$_2$ possesses remarkably enhanced Sommerfeld coefficients, large effective masses, and anomalous transport properties, suggesting a highly renormalized electronic state[13, 18–21]. The large lattice constant and reduced bandwidth in CsFe$_2$As$_2$ enhance the ratio between interaction strength and kinetic energy, driving the system closer to an orbital-selective correlated regime. Previous studies have suggested that CsFe$_2$As$_2$ may approach an orbital-selective Mott phase, where different Fe 3d orbitals exhibit distinct degrees of localization and coherence[5]. In particular, the d_{xy} orbital is expected to experience stronger correlation effects due to its narrower bandwidth and different orbital geometry compared with the $d_{xz/yz}$ orbitals.

The microscopic origin and evolution of electronic coherence in CsFe$_2$As$_2$ remain largely unexplored. Existing angle-resolved photoemission spectroscopy (ARPES) studies have mainly focused on its Fermi surface topology and superconducting properties, while the temperature-dependent evolution of quasiparticle coherence has received much less attention[22, 23]. In strongly correlated systems, the crossover from incoherent excitations at high temperature to coherent quasiparticles at low temperature is expected to manifest itself through characteristic spectral signatures, including the emergence of sharp quasiparticle peaks, redistribution of spectral weight, and temperature-dependent changes in band renormalization. Identifying such signatures provides direct insight into how electronic correlations govern the low-energy excitations.

The concept of coherence-incoherence crossover has been extensively discussed in Hund's metals and other correlated electron systems. Within the DMFT framework, increasing temperature suppresses coherent quasiparticle formation and transfers spectral weight from the quasiparticle peak near the Fermi level to incoherent Hubbard-like features at higher binding energies[6, 24]. Experimentally, this behavior has been observed in several iron-based superconductors through optical spectroscopy, ARPES, and transport measurements[25, 26]. Nevertheless, direct momentum-resolved observation of the coherence-incoherence crossover, particularly in the strongly correlated end member $CsFe_2As_2$, remains lacking.

$CsFe_2As_2$ therefore provides a unique opportunity to investigate how strong electronic correlations influence quasiparticle formation in a multiorbital system. In this work, we employ high-resolution ARPES measurements to investigate the detailed electronic structure and temperature-dependent quasiparticle evolution in $CsFe_2As_2$. By systematically analyzing the band dispersions, spectral weight redistribution, and quasiparticle coherence behavior, we reveal the characteristic signatures associated with a coherence-incoherence crossover. Our results establish $CsFe_2As_2$ as an important platform for studying correlation-driven quasiparticle formation and provide new insights into the role of Hund's coupling and orbital-selective correlations in iron-based superconductors.

II. EXPERIMENTAL METHODS

High-quality single crystals of $CsFe_2As_2$ were grown using the self-flux method[27]. The crystals were characterized by magnetic susceptibility and electrical resistivity measurements (Fig. 1i). A superconducting transition temperature of $T_c = 2.2\,\mathrm{K}$ was observed (inset in Fig. 1i). Considering the resistivity at 300 K and the extracted value at zero temperature, a RRR (residual resistivity ratio) value of 360 is obtained for the measured $CsFe_2As_2$ sample. The measured resistivity-temperature dependence is similar to that reported before[27]. A pronounced crossover appears near 80 K where the slope of resistivity ($d\rho/dT$) changes abruptly as marked by the pink shadow in Fig. 1i.

ARPES measurements were performed using a laser-ARPES system equipped with a 6.994 eV vacuum-ultraviolet (VUV) laser and a DA30L hemispherical electron analyzer[28–30]. The sample was electrically isolated and connected to a Keithley 2450 source meter, enabling application of the sample bias which can significantly expand the accessible mo-

mentum space in laser-ARPES measurements[30]. The laser spot size on the sample surface was focused to approximately 10 μm. For the measurements presented in Figs. 1a-1d, an overall energy resolution of approximately 10 meV was achieved by using a pass energy of 20 eV and a slit width of 0.2 mm under a sample bias of -200 V. A higher energy resolution of approximately 2.5 meV was obtained by using a pass energy of 5 eV and a slit width of 0.2 mm with sample biases of -25 V (Figs. 1e-1f) and 0 V (Figs. 1g, 5, and 6). The angular resolution was better than 0.2° under zero sample bias conditions. All samples were cleaved *in situ* in ultrahigh vacuum with a base pressure better than 5×10^{-11} mbar. The Fermi level of the sample was referenced by measuring a clean polycrystalline gold which is electrically connected to the sample. The work function of $CsFe_2As_2$ was determined to be 1.195 eV by applying a sample bias and then measuring the energy position of the Fermi level and the high binding energy cutoff[30]. Additional synchrotron-based ARPES measurements were carried out at the BL03U endstation of the Shanghai Synchrotron Radiation Facility (SSRF), equipped with a DA30L hemispherical electron analyzer[31] (Fig. 1h). The synchrotron measurements were performed with a pass energy of 10 eV and a slit width of 0.3 mm.

Our first-principle calculations employ the projector augmented wave (PAW) method encoded in Vienna ab initio simulation package (VASP)[32–34]. The Perdew-Burke-Ernzerhof (PBE)[35] exchange-correlation functional is used. In the calculations, the kinetic energy cutoff is set to be 500 eV for the expanding the wave functions into a plane-wave basis, and the Brillouin zone is sampled in the momentum space within a Monkhorst-Pack scheme[36]. On the basis of the equilibrium structure, the momentum mesh used is $7 \times 7 \times 7$. We fix the lattice constants and relax internal atomic positions, and forces are minimized to less than 0.01 eV/Å in the relaxation. We adopt the relax parameters (a=3.894Å, c=14.798Å, z_{As}=0.3355) in the calculations.

III. RESULTS AND DISCUSSION

To establish the complete electronic structure of $CsFe_2As_2$, we first performed comprehensive ARPES measurements to determine its Fermi surface topology and orbital-dependent electronic states. Fig. 1 presents a series of Fermi surface mappings obtained under different experimental conditions, which together reveal the detailed topology and orbital character of

the low-energy electronic states. Fig. 1a-d show the measured Fermi surface mappings from laser ARPES measurements under four different polarization geometries. A large sample bias was applied during these measurements which allows collection of photoelectrons over the 2π solid angle that gives a broad momentum space coverage larger than one Brillouin zone[30]. Different polarization geometries (defined by the slit orientation and the electric field vector($\vec{E}$) of the incident laser as indicated at the left-bottom corners) were used to reveal full electronic structures because the multiple orbitals exhibit quite different photoemission matrix element effects. Since large sample bias tends to degrade the momentum resolution[30], we also carried out laser ARPES measurements using low sample bias (Fig. 1e and Fig. 1f) and zero bias (Fig. 1g) in order to observe fine Fermi surface structures more clearly. To take advantage of photon-energy-dependent matrix element effects to resolve distinct electronic bands, additional synchrotron-based ARPES measurements were performed at a photon energy of $h\nu = 60\,\mathrm{eV}$ (Fig. 1h). Taking together all Fermi surface data acquired under various experimental conditions in Fig. 1a-h, combined with the analysis of the corresponding band structures in Fig. 2 and Fig. 3, we arrived at the measured Fermi surface topology of $CsFe_2As_2$ as depicted in Fig. 1j.

The measured Fermi surface of $CsFe_2As_2$ consists of four hole-like Fermi surface sheets around the Γ point, labeled as α, α', β and γ in Fig. 1j and two hole-like Fermi pockets around the M point, labeled as ε and δ in Fig. 1j. In addition, a small surface state Fermi surface is presented around Γ which is identified by the band structure analysis (Fig. 2b-d). Since the low energy electronic states are mainly from the Fe $3d_{xz}$, $3d_{yz}$ and $3d_{xy}$ orbitals, the measured Fermi surface mappings (Fig. 1) and band structures (Fig. 2 and Fig. 3) exhibit pronounced orbital-dependent matrix element effects. This effect, combined with the multiple band nature and three dimensionality of the band structure, makes the identification of the electronic structures in $CsFe_2As_2$ less straightforward. It also makes it necessary to measure $CsFe_2As_2$ under various conditions using different polarization geometries and different photon energies.

The α Fermi surface exhibits its strongest spectral intensity along Γ-X but is strongly suppressed along Γ-Y in the measurement geometry shown in Fig. 1a and Fig. 1e. The same α Fermi surface shows its strongest spectral intensity along Γ-$M(-\pi,\pi)$ but is strongly suppressed along Γ-$M(\pi,\pi)$ in the measurement geometry shown in Fig. 1c and Fig. 1g. The four-lobed α Fermi surface contour in Fig. 1j is obtained through these measurements.

The α' Fermi surface overlaps with the α Fermi surface along Γ-X and Γ-Y. It can be clearly observed in a special measurement geometry in Fig. 1g where the α' Fermi surface is marked. The β Fermi surface exhibits its strongest spectral intensity along Γ-Y but is strongly suppressed along Γ-X in the measurement geometry shown in Fig. 1a and Fig. 1e. The same β Fermi surface shows its strongest spectral intensity along Γ-X but there are residual spectral weight along Γ-Y and Γ-$M(-\pi,\pi)$ in the measurement geometry shown in Fig. 1f. The four-lobed β Fermi surface contour in Fig. 1j can be obtained through these measurements. The γ Fermi surface is clearly observed in the measurements shown in Fig. 1e and Fig. 1f. The ε Fermi pocket is strongly suppressed in all the laser ARPES measurements (Fig. 1a-d) but it shows up clearly in the synchrotron ARPES measurement shown in Fig. 1h. The δ Fermi pocket around M can be directly observed in Fig. 1a-d although its intensity is weak in the measurements shown in Fig. 1a-b. It shows strongest intensity along Γ-$M(\pi,\pi)$ but is suppressed along Γ-$M(-\pi,\pi)$ in the measurement in Fig. 1c. These results give a hole-like δ Fermi pocket around M as shown in Fig. 1j. The polarization-dependent electronic structure observed here is qualitatively consistent with previous ARPES results on KFe_2As_2[17]. The α, α', and β bands all exhibit characteristic d_{xz}/d_{yz} polarization dependence, indicating substantial d_{xz}/d_{yz} orbital contributions. Meanwhile, the γ-derived band with the most pronounced d_{xy} character forms the largest Fermi pocket.

We note that our high-resolution laser ARPES measurements also uncover subtle weak features in the Fermi surface mappings presented in Fig. 1a-g, which cannot be explained by the Fermi surface topology summarized in Fig. 1j. Several of these features are highlighted by dashed lines in Fig. 1a and Fig. 1f. Scanning tunneling microscopy (STM) experiments on $CsFe_2As_2$ have demonstrated that cleaved surfaces can undergo Cs atomic reconstruction, yielding a $\sqrt{2} \times \sqrt{2}$ surface structure[37]. Analogous to observations on KFe_2As_2[17], such surface reconstruction can induce band folding and thereby generate extra spectral features. Given the relatively strong three-dimensional character of the electronic structure of $CsFe_2As_2$, one cannot rule out the possibility that the finite k_z resolution and simultaneous sampling of multiple different k_z values in laser ARPES measurements may also contribute to these additional signatures. The microscopic origin of these faint features remains an open question and requires further investigation.

To further resolve the low-energy electronic structure associated with the observed Fermi surface, we extracted two momentum cuts along high-symmetry directions from the ARPES

intensity maps. Fig. 2 presents the band structures along Γ-X(Fig. 2a-d) and Γ-M(Fig. 2i-l) obtained from the datasets shown in Fig. 1a-d. The momentum cut positions are indicated in the inset of Fig. 2e and corresponding polarization configurations are shown in the bottom right corner of each figure. To resolve the band structures more clearly, Fig. 2e-h and Fig. 2m-p show corresponding MDC (momentum distribution curve) second derivative images obtained from Fig. 2a-d and Fig. 2i-l, respectively. The observed bands are marked by the corresponding name of the Fermi surface as indicated in Fig. 1j. Similar to the Fermi surface mappings in Fig. 1, the measured band structures also exhibit strong dependence on the measurement geometry. For the $\Gamma - X$ measurements, only the α/α' band(s) is observed using the polarization geometry in Fig. 2a and Fig. 2e. When the measurement geometry is switched to that in Fig. 2b and Fig. 2f, all the SS, α, α', β and γ bands can be observed. In particular, the surface state SS band can be clearly observed in Fig. 2b-d and Fig. 2f-h. This surface state SS band has a weak spectral weight at the Fermi level and therefore it does not show up clearly in the Fermi surface mappings in Fig. 1a-g. For the $\Gamma - M$ measurements, where only part of bands are observed in Fig. 2i,j,l and Fig. 2m,n,p, all the α, β, γ, ε and δ bands show up clearly in Fig. 2k and Fig. 2o. The splitting of the α and α' bands along $\Gamma - M$ is clearly observed in Fig. 2l and Fig. 2p. In particular, the δ band around the M point shows up strongly in all the $\Gamma - M$ measurements in Fig. 2i-l and Fig. 2m-p.

In order to reveal the fine electronic structures of $CsFe_2As_2$ around the zone center, we present in Fig. 3 the laser ARPES measured results with a low sample bias which has a higher momentum resolution. Fig. 3a shows the band structures along seven momentum cuts (Cut1-Cut7) around Γ rotating from Γ-X to Γ-Y. The observed α, α', β and γ bands are marked by the corresponding name of the Fermi surface as indicated in Fig. 1j. In this measurement geometry, mainly the α/α' bands are observed along Cut1 (Γ-X direction) (leftmost panel in Fig. 3a) while the β band shows up strongly in the Cut7 measurement (rightmost panel in Fig. 3a). In between, the γ band is clearly observed along Cut4 and Cut5 and a van Hove singularity (VHS)-like feature appears in the measurement along Cut4 (Γ-M direction). Fig. 3c presents the band structures along six different momentum cuts that are parallel to Γ-X direction but at different k_ys. Again the observed α, α', β and γ bands are marked in the measured band structures. In this case, the α/α' bands show up clearly in the Cut8 and Cut9 measurements while the β band is strong and clear in the Cut11 and Cut12 measurements. The γ band is weak in intensity but can be clearly identified in the

Cut11 and Cut12 measurements. The analysis of the fine band structures in Fig. 3 and the band structures in Fig. 2 is essential in arriving at the Fermi surface topology of $CsFe_2As_2$ as shown in Fig. 1j.

To further elucidate the orbital character and three-dimensional nature of the electronic structure revealed by ARPES, we performed first-principles calculations for $CsFe_2As_2$. The calculated band structure along the high-symmetry momentum paths Γ-M-X-Γ ($k_z = 0$) and Z-A-R-Z ($k_z = 1$) is presented in Fig. 4a, with the bands color-coded according to their Fe $3d$ orbital characters. The calculated Fermi level does not coincide with the experimentally determined chemical potential. To reproduce the experimentally observed Fermi surface topology, the chemical potential is shifted downward by 0.07 eV, such that the experimental Fermi level is located at $E_{\mathrm{F}}(\mathrm{Exp}) = E_{\mathrm{F}} - 0.07\,\mathrm{eV}$, as indicated by the red dashed line. At this energy, multiple bands cross the Fermi level around the Brillouin-zone center and zone corners, giving rise to several Fermi surface sheets with distinct orbital characters and markedly different k_z dispersions. The corresponding three-dimensional Fermi surfaces at $E_{\mathrm{F}}(\mathrm{Exp})$ are shown in Fig. 4b. The calculated Fermi surface sheets around the Brillouin-zone center exhibit a pronounced hierarchy in their dimensionality. The first sheet [Fig. 4b(i)] displays the strongest three-dimensional character. It is concentrated predominantly around $k_z = 1$, whereas no corresponding Fermi surface contour is present at $k_z = 0$, indicating a strong out-of-plane dispersion. In contrast, the second sheet [Fig. 4b(ii)] exhibits the weakest k_z dependence and maintains an almost cylindrical shape throughout the Brillouin zone, characteristic of a predominantly two-dimensional electronic structure. The third sheet [Fig. 4b(iii)] also extends continuously along k_z, but its cross-sectional size varies appreciably between $k_z = 0$ and $k_z = 1$, resulting in a moderately warped cylindrical morphology. It therefore retains a quasi-two-dimensional character while exhibiting appreciable three-dimensional dispersion. The fourth sheet [Fig. 4b(iv)] has a considerably more complex topology. Around the Brillouin-zone center, it forms a strongly warped Γ-centered sheet whose cross-sectional size and shape evolve substantially with k_z. In addition, two distinct types of Fermi surface pockets emerge around the zone corners. The pocket closest to the M point is confined to a narrow region near $k_z = 0$ and rapidly disappears upon moving away from this plane, indicating a strongly three-dimensional character. By contrast, the outer M-centered pocket persists continuously from $k_z = 0$ to $k_z = 1$, although its size and shape evolve with k_z. It therefore forms a more extended Fermi surface sheet along the out-of-

plane direction. Thus, the fourth sheet consists of a strongly warped Γ-centered component together with two M-centered pockets exhibiting markedly different k_z dispersions. The evolution of these Fermi surface sheets along the out-of-plane direction is further illustrated by the constant-k_z contours shown in Figs. 4c and d. At $k_z = 0$, several concentric hole-like contours are present around Γ, accompanied by additional pockets around the four M points. Upon moving to $k_z = 1$, the central Fermi surface contours undergo substantial changes in both size and shape, directly reflecting the finite k_z warping of the corresponding bands. The strongly three-dimensional first sheet emerges around the Z point at $k_z = 1$, while the zone-corner pockets evolve into the corresponding structures around the A points. Notably, the pocket located closest to M at $k_z = 0$ has no appreciable counterpart at $k_z = 1$, consistent with its confinement to a narrow range of k_z near the $k_z = 0$ plane. In contrast, the outer zone-corner pocket survives throughout the $k_z = 0 - 1$ interval. These calculations therefore demonstrate that the Fermi surface sheets of $CsFe_2As_2$ possess strongly band-dependent dimensionalities, ranging from nearly two-dimensional cylinders to highly three-dimensional and strongly warped structures.

This pronounced k_z dependence is particularly important for interpreting the low-photon-energy ARPES measurements. Owing to the low photon energy and the small work function of $CsFe_2As_2$, the photoelectrons detected in our 6.994-eV laser-ARPES measurements span a finite range of out-of-plane momentum within a single Brillouin zone. Using an inner potential of $V_0 = 12\,\text{eV}$[23] and a work function of $1.2\,\text{eV}$[29], we estimate that the nominal k_z at the zone center probed by the 6.994-eV laser is close to the Z point ($k_z = 1$), whereas the zone-corner measurements correspond approximately to the M point ($k_z = 0$). The resulting k_z assignment provides a natural basis for directly comparing the calculated Fermi surfaces with the experimentally observed topology. Indeed, the calculation reproduces several key features of the experimentally observed Fermi surface. Around the Z point, four hole-like Fermi surface sheets are predicted, while a small hole pocket is found around the M point and is surrounded by a four-lobed, petal-like Fermi surface structure. These features are in good qualitative agreement with the Fermi surface topology observed in our 6.994-eV laser-ARPES measurements. The overall agreement indicates that the calculated band structure captures the gross topology and three-dimensional character of the low-energy electronic structure, and further supports the assignment of the laser-ARPES measurements to the corresponding k_z regions. Despite this qualitative agreement in Fermi surface topology, a

pronounced discrepancy emerges in the orbital composition of the individual Fermi surface sheets. In the calculation, the innermost Fermi pocket around the Γ point is predominantly derived from the d_{xy} orbital, whereas the second and fourth pockets exhibit dominant d_{z^2} character. Only the third pocket is primarily composed of the d_{xz} and d_{yz} orbitals. This orbital distribution is in clear contrast to the polarization-dependent ARPES measurements. Experimentally, the α, α', and β bands possess substantial d_{xz}/d_{yz} orbital contributions and the γ band is mainly from the d_{xy} orbital. Thus, although the calculations reproduce the number and overall topology of the Fermi surface sheets, they fail to capture their experimentally observed orbital hierarchy.

The polarization-dependent electronic structure observed here differs distinctly from the orbital assignment obtained in conventional first-principles calculations. This discrepancy suggests that the orbital composition of the low-energy electronic states is substantially renormalized by electronic correlations. Given the strong correlation effects manifested in the transport properties of $CsFe_2As_2$, conventional uncorrelated calculations can therefore provide only a qualitative description of the experimentally observed Fermi surface topology. In particular, they reproduce the overall number and approximate geometry of the Fermi surface sheets, but fail to accurately capture their detailed orbital compositions and associated band dispersions. This discrepancy between the calculated and experimentally resolved orbital characters provides important evidence that correlation effects play a crucial role in determining the low-energy electronic structure of $CsFe_2As_2$.

The combined polarization-dependent Fermi surface mapping and detailed momentum cuts establish that $CsFe_2As_2$ hosts a strongly anisotropic multiorbital electronic structure. The multiple hole-like pockets around the Γ point possess distinct orbital characters. Such orbital differentiation is a central characteristic of strongly correlated iron-based superconductors and provides an essential background for understanding the subsequent temperature-dependent quasiparticle evolution. In particular, the coexistence of multiple renormalized hole bands with different orbital characters allows us to investigate whether electronic coherence evolves uniformly across different electronic states or exhibits orbital-dependent behavior. The well-resolved α and β bands, with their distinct polarization dependence and comparable momentum locations, provide an ideal platform for tracking the evolution of quasiparticle coherence as a function of temperature. The resistivity anomaly near 80 K suggests a crossover in the electronic scattering behavior[19–21], but transport measurements

alone cannot reveal the microscopic origin of this evolution. We use temperature-dependent laser-ARPES measurements to directly track the evolution of low-energy quasiparticle excitations. We focus on the α and β bands because both exhibit well-defined hole-like dispersions near the Fermi level.

Figure 5 presents the temperature evolution of the inner hole pocket α measured by laser ARPES from 200 K down to 16 K. To minimize possible aging effects associated with the highly reactive Cs atoms, the temperature-dependent measurements were performed during cooling rather than heating process. To avoid sample shifting or slight orientation change during temperature variation, at each temperature, the Fermi surface mapping was carried out around the measured momentum cut. Fig. 5a shows the band structures measured at different temperatures along a momentum cut crossing the α pocket along the Γ-X direction. At low temperatures, the α band exhibits a sharp and well-defined hole-like dispersion crossing the Fermi level, indicating the presence of coherent quasiparticle excitations. Upon increasing temperature, the band gradually broadens and loses spectral intensity. However, the quasiparticle feature remains observable even at 200 K, demonstrating that the loss of coherence occurs continuously rather than through an abrupt disappearance of the band.

Figure 5c shows momentum distribution curves (MDCs) at E_F measured at different temperatures. At low temperatures, the MDC peaks are sharp. These MDC peaks obviously get broadened at high temperatures. The two MDC peaks are fitted by two Lorentzians and the extracted temperature-dependent Fermi momentum is plotted in Fig. 5e. The extracted temperature dependence of the corresponding MDC width and MDC height is presented in Fig. 5f. Two sets of the Fermi momentum, MDC width and MDC height can be obtained by fitting the two MDC peaks of the left and right sides of the α band and the averaged values are shown in Fig. 5e and Fig. 5f. A notable temperature dependence is observed in the Fermi momentum. k_F^{α} decreases continuously with increasing temperature from 16 K to 85 K and then slightly increases with increasing temperature from 85 K to 200 K. The change of the Fermi momentum from 16 K to 85 K reaches $\sim$20%. Such a temperature-dependent shift of the Fermi momentum is unusual because the Fermi surface volume of a conventional metal is generally insensitive to temperature. Similar temperature-induced Fermi momentum shift is reported in other iron-based superconductors[38–40]. In the meantime, the MDC height (green solid squares in Fig. 5f) also exhibits a rapid decrease with increasing temperature from 16 K to $\sim$50 K and then changes only slightly from 50 K to 200 K. The MDC width

(black solid triangles in Fig. 5f) shows a rapid increase with increasing temperature from 0.09 π/a at 16 K to 0.17 π/a at 50 K but it keeps growing with increasing temperature from 0.17 π/a at 50 K to 0.25 π/a at 200 K. The relative change is significant that amounts to 90% increase from 16 K to 50 K and even up to 180% increase from 16 K to 200 K. These results clearly indicate a crossover from low temperature coherence to high temperature incoherence that occurs around 50∼85 K.

The temperature-induced coherence-incoherence crossover also shows up in EDCs. Fig. 5d shows EDCs at the Fermi momentum measured at different temperatures. It is clear that the EDCs show sharp coherent peaks at low temperatures but they get much broadened at high temperatures. To analyze these EDCs quantitatively, the EDCs are symmetrized with respect to the Fermi level and the symmetrized EDCs are fitted by a Lorentzian to get the symmetrized EDC width and symmetrized EDC height that are plotted in Fig. 5g. The symmetrized EDC height (green empty squares in Fig. 5g) exhibits a rapid decrease with increasing temperature from 16 K to ∼50 K and then decreases slowly from 50 K to 200 K. This is consistent with the loss of sharp EDC peaks with increasing temperature shown in Fig. 5d. Correspondingly, the symmetrized EDC width (black empty triangles in Fig. 5g) keeps increasing with increasing temperature from 28 meV at 16 K to 155 meV at 200 K.

Figure 5h presents the temperature dependence of the Fermi velocity for the α band. The Fermi velocity is obtained by MDC fitting of the α bands in Fig. 5a and getting the slope of the E-k dispersion near the Fermi level. The Fermi velocity extracted from the left α band (red solid circles) and the right α band (blue solid squares) is identical. Overall the Fermi velocity of the α band is small and it exhibits a minimum around 40∼60 K. With decreasing temperature from 200 K to 40 K, the Fermi velocity decreases from 0.81 eV·Å to 0.46 eV·Å corresponding to a gradual flattening of the α band with decreasing temperature seen in Fig. 5a. From the Fermi momentum and the Fermi velocity, one can get the effective mass $m^* = \hbar k_F/v_F$ which is plotted in Fig. 5i. The effective mass is found to increase with the decreasing temperature, from 1.8 at 200 K to 3.5 at 16 K. This indicates the enhancement of electron correlation with decreasing temperature for the α band.

Now we turn to examine the temperature dependence of the β band. Fig. 6 presents the temperature evolution of the middle hole pocket β measured by laser ARPES from 200 K down to 16 K. Fig. 6a shows the band structures measured at different temperatures along a momentum cut crossing the β pocket along the Γ-X direction. At low temperatures,

the β band exhibits a sharp and well-defined hole-like dispersion crossing the Fermi level. Upon increasing temperature, the band gradually broadens and loses spectral intensity. Fig. 6c presents MDCs at E_F measured at different temperatures obtained from Fig. 6a. The MDCs show two sharp peaks at low temperatures. These MDC peaks get broadened with increasing temperature and become nearly invisible at high temperatures. To analyze these MDCs quantitatively, the two peaks are fitted by two Lorentzians and the extracted temperature-dependent Fermi momentum is plotted in Fig. 6e. The extracted temperature dependence of the corresponding MDC width and MDC height is presented in Fig. 6f. The Fermi momentum, MDC width and MDC height shown in Fig. 6e and Fig. 6f are averaged values obtained by fitting the two MDC peaks of the left and right sides of the β band. Overall, the Fermi momentum of the β band k_F^{β} shows a gradual decrease with increasing temperature from 16 K to 200 K. But the MDC height (green solid squares in Fig. 6f) exhibits a rapid decrease with increasing temperature from 16 K to $\sim$50 K and then changes only slightly from 50 K to 200 K. On the other hand, the MDC width (black solid triangles in Fig. 6f) first shows a rapid increase with increasing temperature from 0.12 π/a at 16 K to 0.22 π/a at 60 K and then slightly decreases with the temperature increase from 60 K to 200 K. The rapid decrease of the MDC height and the rapid increase of the MDC width from 16 K to 50$\sim$60 K are consist with the rapid loss of two peaks in MDCs as shown in Fig. 6c. These results clearly demonstrate a crossover from low-temperature coherence to high-temperature incoherence near 50$\sim$60 K.

The coherence-incoherence crossover of the β band can be more directly observed in EDCs. Fig. 6d shows EDCs at the Fermi momentum of the β band measured at different temperatures. It is clear that the EDCs show sharp coherent peaks at low temperatures but the coherent peak gets broadened with increasing temperature and becomes nearly invisible at high temperatures. To analyze these EDCs quantitatively, the EDCs are symmetrized with respect to the Fermi level and the symmetrized EDCs are fitted by a Lorentzian to get the symmetrized EDC width and symmetrized EDC height that are plotted in Fig. 6g. The symmetrized EDC height (green empty squares in Fig. 6g) exhibits a rapid decrease with increasing temperature from 16 K to $\sim$50 K and then decreases slowly from 50 K to 200 K. This is consistent with the loss of sharp EDC peaks with increasing temperature shown in Fig. 6d. Correspondingly, the symmetrized EDC width (black empty triangles in Fig. 6f) keeps increasing with increasing temperature from 39 meV at 16 K to 264 meV at 200 K.

Fig. 6h presents the temperature dependence of the Fermi velocity for the β band. Overall the Fermi velocity of the β band is small and shows little change with temperature. In the meantime, the effective mass (Fig. 6i) also shows little change with temperature.

We systematically resolve the low-energy electronic structure of $CsFe_2As_2$ via polarization-resolved laser and synchrotron ARPES measurements. The observed Fermi surface consists of multiple hole-like pockets around the Γ and M points with distinct orbital characters, dominated by Fe $3d_{xz/yz}$ and $3d_{xy}$ orbitals. The strong polarization-dependent spectral responses confirm the multi-orbital and highly anisotropic nature of the low-energy electronic states in this heavily hole-doped iron pnictide. Complementary first-principles calculations further validate and enrich this experimental electronic structure picture. The theoretical results reveal pronounced three-dimensionality and strong k_z dispersion in $CsFe_2As_2$, with largely modulated Fermi surface topology evolving from $k_z = 0$ to $k_z = 1$. The calculated multi-orbital band structure and 3D Fermi surface morphology are in excellent overall agreement with our ARPES observations. Such intrinsic 3D multi-band characteristics lay the fundamental structural basis for the complex quasiparticle dynamical behaviors and orbital-selective correlation effects observed in temperature-dependent measurements.

On the basis of this validated electronic structure, our temperature-dependent ARPES measurements uncover prominent orbital-selective coherence-incoherence crossover behavior in $CsFe_2As_2$. Both of the dominant $d_{xz/yz}$-derived α and β bands undergo universal thermally induced quasiparticle dephasing around 50-60 K, demonstrating a generic coherence breakdown of low-energy coherent quasiparticles in the system. Despite their identical orbital parentage and consistent crossover temperature scale, the two bands exhibit fundamentally distinct high-temperature quasiparticle evolution. The β band experiences complete coherence quenching above 50-60 K, with nearly vanishing coherent spectral weight, while its Fermi momentum, Fermi velocity and effective mass remain nearly temperature independent, indicating full quasiparticle dephasing without noticeable modification of intrinsic band dispersion. In contrast, the α band only suffers partial coherence degradation. Although its spectral weight and Fermi momentum are substantially suppressed across the crossover regime, residual coherent quasiparticle peaks persist up to 200 K, accompanied by continuous monotonic broadening of spectral linewidths. This divergent sustainability of coherent states between bands highlights the strong band-selective correlation effect in $CsFe_2As_2$.

Such band-dependent coherence evolution is a characteristic hallmark of strongly correlated multi-orbital systems. Different from conventional metals with homogeneous quasiparticle responses and temperature-stable Fermi surfaces, correlated iron-based systems allow distinct correlation strengths and scattering rates even for bands with the same dominant orbital character. Subtle differences in orbital hybridization and local electronic localization naturally lead to the orbital-selective coherence-incoherence crossover observed in $CsFe_2As_2$. Our joint theory and experiment results provide a microscopic interpretation of the normal-state transport anomaly in $CsFe_2As_2$. The macroscopic resistivity kink near 80 K originates from the broad-range partial coherence degradation of the α band within 50-85 K, while the sharp full dephasing of the β band at 50-60 K further regulates electronic scattering, establishing a direct microscopic-macroscopic correlation.

Compared with isostructural KFe_2As_2, the unique 3D electronic structure and orbital-selective crossover behavior of $CsFe_2As_2$ demonstrate that slight chemical and lattice variations can effectively tune orbital correlations and quasiparticle coherence in heavily hole-doped iron pnictides. Minor residual spectral features in Fermi surface maps are likely attributed to surface reconstruction and finite k_z sampling effects, which deserve further investigation. Overall, this work provides a comprehensive understanding of correlation-driven orbital-selective quasiparticle dynamics in iron-based superconductors.

IV. SUMMARY

In summary, we combine first-principles calculations and comprehensive polarization-resolved ARPES measurements to systematically investigate the electronic structure and temperature-dependent quasiparticle evolution of $CsFe_2As_2$. Theoretical calculations confirm the highly three-dimensional, multi-orbital Fermi surface geometry and strong k_z dispersion of $CsFe_2As_2$, which is qualitatively consistent with our experimental laser and synchrotron ARPES results. Temperature-dependent spectroscopic measurements reveal a universal coherence-incoherence crossover around 50-60 K for both $d_{xz/yz}$-derived α and β bands, yet with dramatically different high-temperature behaviors. The β band undergoes complete quasiparticle dephasing and loses all coherent spectral features at high temperature, while the α band retains residual coherent quasiparticle peaks despite significant spectral suppression. This distinct band-selective coherence evolution microscopically ac-

counts for the normal-state transport anomaly near 80 K. Our joint theory-experiment work provides definitive spectroscopic evidence for orbital-selective correlation effects in heavily hole-doped iron-based superconductors, advancing the fundamental understanding of multi-orbital quasiparticle dynamics and coherence crossover in strongly correlated electron systems.

*Corresponding author: LZhao@iphy.ac.cn, XJZhou@iphy.ac.cn.

---

[1] J. Paglione and R. L. Greene. High-temperature superconductivity in iron-based materials. *Nat. Phys.*, 6(9):645–658, 2010.

[2] G. R. Stewart. Superconductivity in iron compounds. *Rev. Mod. Phys.*, 83(4):1589–1652, 2011.

[3] H. Hosono and K. Kuroki. Iron-based superconductors: Current status of materials and pairing mechanism. *Physica C*, 514:399–422, 2015.

[4] R. M. Fernandes, A. I. Coldea, H. Ding, I. R. Fisher, P. J. Hirschfeld, and G. Kotliar. Iron pnictides and chalcogenides: a new paradigm for superconductivity. *Nature*, 601(7891):35–44, 2022.

[5] Z. P. Yin, K. Haule, and G. Kotliar. Kinetic frustration and the nature of the magnetic and paramagnetic states in iron pnictides and iron chalcogenides. *Nat. Mater.*, 10(12):932–935, 2011.

[6] A. Georges, L. de' Medici, and J. Mravlje. Strong correlations from Hund's coupling. *Annu. Rev. Condens. Matter Phys.*, 4(1):137–178, 2013.

[7] Z. P. Yin, K. Haule, and G. Kotliar. Magnetism and charge dynamics in iron pnictides. *Nat. Phys.*, 7(4):294–297, 2011.

[8] M. Rotter, M. Tegel, and D. Johrendt. Superconductivity at 38 K in the iron arsenide $(Ba_{1-x}K_x)Fe_2As_2$. *Phys. Rev. Lett.*, 101(10):107006, 2008.

[9] A. E. Böhmer, F. Hardy, L. Wang, T. Wolf, P. Schweiss, and C. Meingast. Superconductivity-induced re-entrance of the orthorhombic distortion in $Ba_{1-x}K_xFe_2As_2$. *Nat. Commun.*, 6(1):7911, 2015.

[10] Z. Bukowski, S. Weyeneth, R. Puzniak, J. Karpinski, and B. Batlogg. Bulk superconductivity

at 2.6 K in undoped $RbFe_2As_2$. *Physica C*, 470:S328–S329, 2010.

[11] Z. Zhang, A. F. Wang, X. C. Hong, J. Zhang, B. Y. Pan, J. Pan, Y. Xu, X. G. Luo, X. H. Chen, and S. Y. Li. Heat transport in $RbFe_2As_2$ single crystals: Evidence for nodal superconducting gap. *Phys. Rev. B*, 91(2):024502, 2015.

[12] K. Sasmal, B. Lv, B. Lorenz, A. M. Guloy, F. Chen, Y.Y. Xue, and C.W. Chu. Superconducting Fe-based compounds $(A_{1-x}Sr_x)Fe_2As_2$ with A = K and Cs with transition temperatures up to 37 K. *Phys. Rev. Lett.*, 101(10):107007, 2008.

[13] A. F. Wang, B. Y. Pan, X. G. Luo, F. Chen, Y. J. Yan, J. J. Ying, G. J. Ye, P. Cheng, X. C. Hong, S. Y. Li, and X. H. Chen. Calorimetric study of single-crystal $CsFe_2As_2$. *Phys. Rev. B*, 87(21):214509, 2013.

[14] S. Backes, H. O. Jeschke, and R. Valenti. Microscopic nature of correlations in multiorbital AFe_2As_2 (A = K, Rb, Cs): Hund's coupling versus coulomb repulsion. *Phys. Rev. B*, 92(19):195128, 2015.

[15] F. Hardy, A. E. Böhmer, L. de' Medici, M. Capone, G. Giovannetti, R. Eder, L. Wang, M. He, T. Wolf, P. Schweiss, R. Heid, A. Herbig, P. Adelmann, R. A. Fisher, and C. Meingast. Strong correlations, strong coupling, and s-wave superconductivity in hole-doped $BaFe_2As_2$ single crystals. *Phys. Rev. B*, 94(20):205113, 2016.

[16] T. Yoshida, S. I. Ideta, I. Nishi, A. Fujimori, M. Yi, R. G. Moore, S. K. Mo, D. Lu, Z. X. Shen, Z. Hussain, K. Kihou, P. M. Shirage, H. Kito, C. H. Lee, A. Iyo, H. Eisaki, and H. Harima. Orbital character and electron correlation effects on two-and three-dimensional Fermi surfaces in KFe_2As_2 revealed by angle-resolved photoemission spectroscopy. *Front. Phys.*, 2:17, 2014.

[17] D. S. Wu, J. J. Jia, J. G. Yang, W. S. Hong, Y. J. Shu, T. M. Miao, H. T. Yan, H. T. Rong, P. Ai, X. Zhang, C. H. Yin, J. Y. Liu, H. K. Chen, Y. H. Yang, C. Peng, C. L. Li, S. J. Zhang, F. F. Zhang, F. Yang, Z. M. Wang, N. Zong, L. J. Liu, R. K. Li, X. Y. Wang, Q. J. Peng, H. Q. Mao, G. D. Liu, S. L. Li, Y. L. Chen, H. Q. Luo, X. X. Wu, Z. Y. Xu, L. Zhao, and X. J. Zhou. Nodal s± pairing symmetry in an iron-based superconductor with only hole pockets. *Nat. Phys.*, 20(4):571–578, 2024.

[18] F. Eilers, K. Grube, D. A. Zocco, T. Wolf, M. Merz, P. Schweiss, R. Heid, R. Eder, R. Yu, J. X. Zhu, Q. Si, T. Shibauchi, and H. V. Lohneysen. Strain-driven approach to quantum criticality in AFe_2As_2 with A=K, Rb, and Cs. *Phys. Rev. Lett.*, 116(23):237003, 2016.

[19] Y. P. Wu, D. Zhao, A. F. Wang, N. Z. Wang, Z. J. Xiang, X. G. Luo, T. Wu, and X. H.

Chen. Emergent Kondo lattice behavior in iron-based superconductors AFe_2As_2 (A=K, Rb, Cs). *Phys. Rev. Lett.*, 116(14):147001, 2016.

[20] Z. J. Xiang, N. Z. Wang, A. F. Wang, D. Zhao, Z. L. Sun, X. G. Luo, T. Wu, and X. H. Chen. Incoherence-coherence crossover and low-temperature Fermi-liquid-like behavior in AFe_2As_2 (A = K, Rb, Cs): evidence from electrical transport properties. *J. Phys.: Condens. Matter*, 28(42):425702, 2016.

[21] P. Wiecki, A. A. Haghighirad, F. Weber, M. Merz, R. Heid, and A. E. Böhmer. Dominant in-plane symmetric elastoresistance in $CsFe_2As_2$. *Phys. Rev. Lett.*, 125(18):187001, 2020.

[22] S. Kong, D. Y. Liu, S. T. Cui, S. L. Ju, A. F. Wang, X. G. Luo, L. J. Zou, X. H. Chen, G. B. Zhang, and Z. Sun. Electronic structure in a one-Fe Brillouin zone of the iron pnictide superconductors $CsFe_2As_2$ and $RbFe_2As_2$. *Phys. Rev. B*, 92(18):184512, 2015.

[23] P. Richard, A. van Roekeghem, X. Shi, P. Seth, B. Q. Lv, K. Kim, X. H. Chen, S. Biermann, and H. Ding. Van Hove singularities, chemical pressure and phonons: an angle-resolved photoemission study of KFe_2As_2 and $CsFe_2As_2$. arXiv:arXiv:1807.00193, 2018.

[24] L. de' Medici. Hund's induced Fermi-liquid instabilities and enhanced quasiparticle interactions. *Phys. Rev. Lett.*, 118(16):167003, 2017.

[25] H. Miao, Z. P. Yin, S. F. Wu, J. M. Li, J. Ma, B. Q. Lv, X. P. Wang, T. Qian, P. Richard, L. Y. Xing, X. C. Wang, C. Q. Jin, K. Haule, G. Kotliar, and H. Ding. Orbital-differentiated coherence-incoherence crossover identified by photoemission spectroscopy in LiFeAs. *Phys. Rev. B*, 94(20):201109, 2016.

[26] F. Hardy, A. E. Böhmer, D. Aoki, P. Burger, T. Wolf, P. Schweiss, R. Heid, P. Adelmann, Y. X. Yao, G. Kotliar, J. Schmalian, and C. Meingast. Evidence of strong correlations and coherence-incoherence crossover in the iron pnictide superconductor KFe_2As_2. *Phys. Rev. Lett.*, 111(2):027002, 2013.

[27] A. F. Wang, B. Y. Pan, X. G. Luo, F. Chen, Y. J. Yan, J. J. Ying, G. J. Ye, P. Cheng, X. C. Hong, S. Y. Li, and X. H. Chen. Calorimetric study of single-crystal $CsFe_2As_2$. *Phys. Rev. B*, 87(21):214509, 2013.

[28] G. D. Liu, G. L. Wang, Y. Zhu, H. B. Zhang, G. C. Zhang, X. Y. Wang, Y. Zhou, W. T. Zhang, H. Y. Liu, L. Zhao, J. Q. Meng, X. L. Dong, C. T. Chen, Z. Y. Xu, and X. J. Zhou. Development of a vacuum ultraviolet laser-based angle-resolved photoemission system with a superhigh energy resolution better than 1 meV. *Rev. Sci. Instrum.*, 79(2):023105, 2008.

[29] X. J. Zhou, S. L. He, G. D. Liu, L. Zhao, L. Yu, and W. T. Zhang. New developments in laser-based photoemission spectroscopy and its scientific applications: a key issues review. *Rep. Prog. Phys.*, 81(6):062501, 2018.

[30] T. M. Miao, Y. Xu, B. Liang, W. P. Zhu, N. Cai, M. K. Xu, D. Wu, H. Z. Gu, W. J. Mao, S. J. Zhang, F. F. Zhang, F. Yang, Z. M. Wang, Q. J. Peng, Z. Y. Xu, Z. H. Zhu, X. T. Li, H. Q. Mao, L. Zhao, G. D. Liu, and X. J. Zhou. Expansion of momentum space and full 2π solid angle photoelectron collection in laser-based angle-resolved photoemission spectroscopy by applying sample bias. *Rev. Sci. Instrum.*, 97(3):033908, 2026.

[31] Y. C. Yang, Z. T. Liu, J. S. Liu, Z. H. Liu, W. L. Liu, X. L. Lu, H. P. Mei, A. Li, M. Ye, S. Qiao, and D. W. Shen. High-resolution ARPES endstation for in situ electronic structure investigations at SSRF. *Nucl. Sci. Tech.*, 32(3):31, 2021.

[32] G. Kresse and J. Hafner. Ab initio molecular dynamics for liquid metals. *Phys. Rev. B*, 47(1):558–561, 1993.

[33] G. Kresse and J. Furthmüller. Efficiency of ab-initio total energy calculations for metals and semiconductors using a plane-wave basis set. *Comput. Mater. Sci.*, 6(1):15–50, 1996.

[34] G. Kresse and J. Furthmüller. Efficient iterative schemes for ab initio total-energy calculations using a plane-wave basis set. *Phys. Rev. B*, 54(16):11169–11186, 1996.

[35] J. P. Perdew, K. Burke, and M. Ernzerhof. Generalized gradient approximation made simple. *Phys. Rev. Lett.*, 77(18):3865–3868, 1996.

[36] H. J. Monkhorst and J. D. Pack. Special points for Brillouin-zone integrations. *Phys. Rev. B*, 13(12):5188–5192, 1976.

[37] X. Yang, Z. Y. Du, H. Lin, D. L. Fang, H. Yang, X. Y. Zhu, and H. H. Wen. Vortex lattice and vortex bound states in $CsFe_2As_2$ investigated by scanning tunneling microscopy/spectroscopy. *Phys. Rev. B*, 98(2):024505, 2018.

[38] V. Brouet, P. H. Lin, Y. Texier, J. Bobroff, A. TalebIbrahimi, P. Le Fèvre, F. Bertran, M. Casula, P. Werner, S. Biermann, F. RullierAlbenque, A. Forget, and D. Colson. Large temperature dependence of the number of carriers in codoped $BaFe_2As_2$. *Phys. Rev. Lett.*, 110(16):167001, 2013.

[39] R. S. Dhaka, S. E. Hahn, E. Razzoli, R. Jiang, M. Shi, B. N. Harmon, A. Thaler, S. L. Bud'ko, P. C. Canfield, and A. Kaminski. Unusual temperature dependence of band dispersion in $Ba(Fe_{1-x}Ru_x)_2As_2$ and its consequences for antiferromagnetic ordering. *Phys. Rev. Lett.*,

110(6):067002, 2013.

[40] P. H. Lin, Y. Texier, A. TalebIbrahimi, P. Le Fèvre, F. Bertran, E. Giannini, M. Grioni, and V. Brouet. Nature of the bad metallic behavior of $Fe_{1.06}Te$ inferred from its evolution in the magnetic state. *Phys. Rev. Lett.*, 111(21):217002, 2013.

Acknowledgement

We thank Zhengtai Liu and Mao Ye for providing the experimental support for the measurements performed on BL03U in SSRF. This work is supported by the National Natural Science Foundation of China (Grant Nos. 12488201 by X.J.Z., 12374066 by L.Z. and 12374154 by X.T.L.), the National Key Research and Development Program of China (Grant Nos. 2021YFA1401800 by X.J.Z., 2022YFA1604200 by L.Z., 2022YFA1403900 by G.D.L. and 2023YFA1406000 by X.T.L.), CAS Superconducting Research Project (Grant No. SCZX-0101), Innovation Program for Quantum Science and Technology (Grant No. 2021ZD0301800 by X.J.Z.), the Youth Innovation Promotion Association of CAS (Grant No. Y2021006 by L.Z.) and the Synergetic Extreme Condition User Facility (SECUF). S.L.L. acknowledges support from the National Key Research and Development Program of China (Grant Nos. 2022YFA1403400 and 2021YFA1400400). X.X.W. acknowledges support from the National Key R&D Program of China (Grant No. 2023YFA1407300) and the National Natural Science Foundation of China (Grants No. 12574151, 12447103 and 12447101).

Author Contributions

X.J.Z., L.Z. and Y.J.S. proposed and designed the research. H.L.Z., H.Q.L and S.L.L. contributed in sample growth and the magnetic and resistivity measurements. Y.J.S., J.C.W., T.M.M., J.X.Z., B.L., W.P.Z., N.C, M.K.X., Y.W.C., J.M.S., S.J.Z., F.F.Z., F.Y., Z.M.W., Q.J.P., Z.Y.X., M.H.Q., Z.H.Z., X.T.L., G.D.L., L.Z. and X.J.Z. contributed to the development and maintenance of the ARPES systems and related software development. Y.J.S. and J.C.W. carried out the ARPES experiments. C.C.L. and X.X.W. contributed to the band structure calculations. X.J.Z., L.Z. and Y.J.S. analyzed the data and wrote the paper. All authors participated in discussions and comments on the paper.

Competing Interests Statement

The authors declare that they have no competing financial interests.

Additional information

Correspondence and requests for materials should be addressed to L. Zhao and X. J. Zhou.

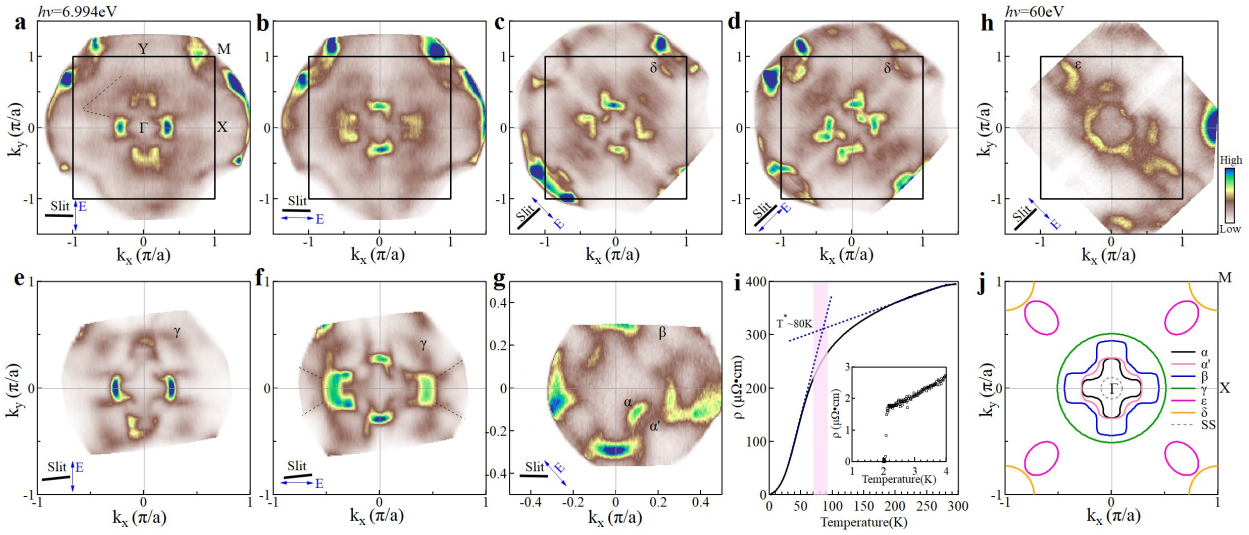


FIG. 1. **Fermi surface of $CsFe_2As_2$ measured under different conditions.** **(a-d)**, Fermi surface mappings of $CsFe_2As_2$ measured at 16 K by laser ARPES under different polarization geometries. The polarization geometry is defined by the slit orientation and the electric field vector($\vec{E}$) of the incident laser as indicated at the left-bottom corners. To increase the momentum space coverage, a sample bias voltage of -200 V was applied during the measurements. These mappings are obtained by integrating the spectral intensity within ± 1 meV with respect to the Fermi level. The first Brillouin zone is marked by a black line square. **(e-f)**, Fermi surface mappings of $CsFe_2As_2$ measured at 18 K by laser ARPES under two different polarization geometries. A sample bias voltage of -25 V was applied during the measurements. **(g)**, Fermi surface mapping near the zone center Γ point measured at 15 K by laser ARPES. No sample bias was applied during the measurement. **(h)**, Fermi surface mapping measured at 13 K by synchrotron-based ARPES with a photon energy of 60 eV. **(i)**, In-plane electrical resistivity ρ of $CsFe_2As_2$ measured from 2 to 300 K. A pronounced crossover appears near 80 K where the slope of resistivity ($d\rho/dT$) changes abruptly as marked by the pink shadow. The inset shows the zoom-in of the low-temperature region where a sharp superconducting transition at $T_c \approx 2.2\,K$ is observed. **(j)**, Fermi surface of $CsFe_2As_2$ obtained by analyzing the Fermi surface mappings and band structures measured under different conditions.

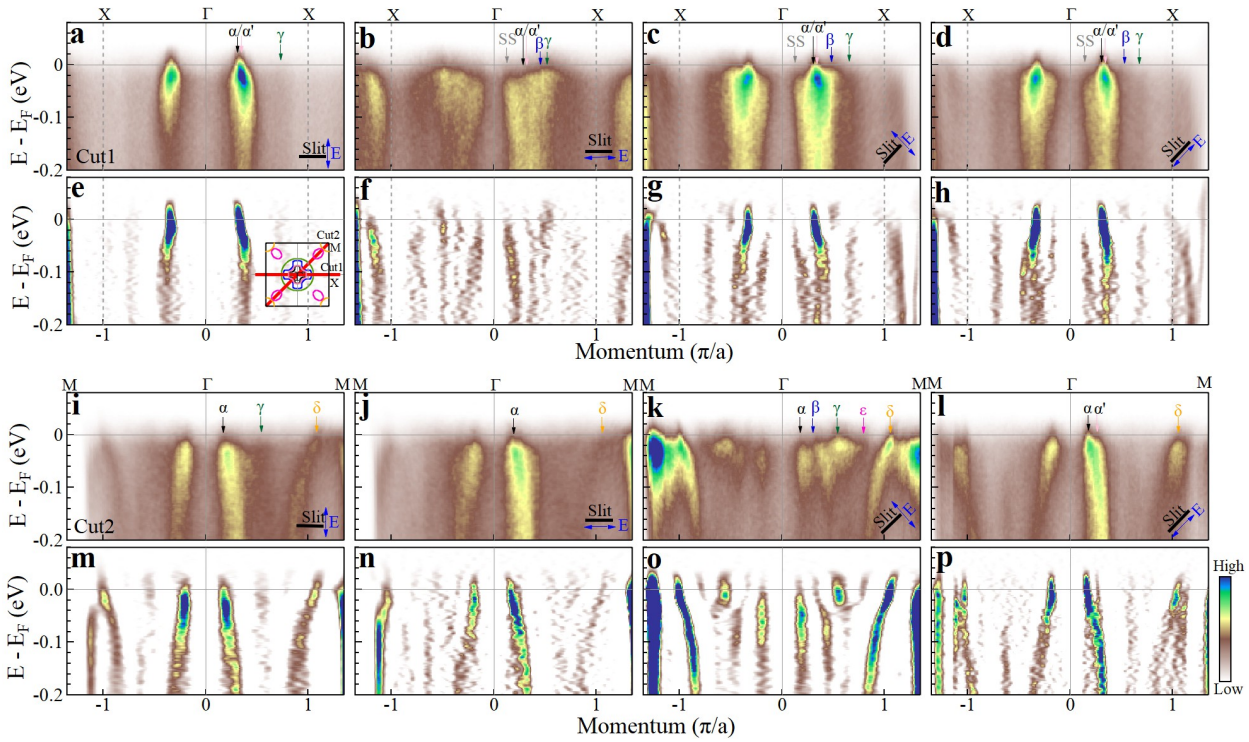


FIG. 2. **Band structures of $CsFe_2As_2$ along two high-symmetry directions measured at 16 K under different polarization geometries. These are obtained from the same measurements shown in Fig. 1a – d. (a-d)**, Band structures measured along $\Gamma - X$ direction (momentum cut Cut1) under different polarization geometries. **(e-f)**, Corresponding MDC second derivative images obtained from **a – d**. **(i-l)**, Band structures measured along $\Gamma - M$ direction (momentum cut Cut2) under different polarization geometries. **(m-p)**, Corresponding MDC second derivative images obtained from **i – l**. The location of the momentum cuts Cut1 and Cut2 is marked by red lines in the inset of **e**. The observed bands are labeled by the corresponding name of the Fermi surface as indicated in Fig. 1**j**.

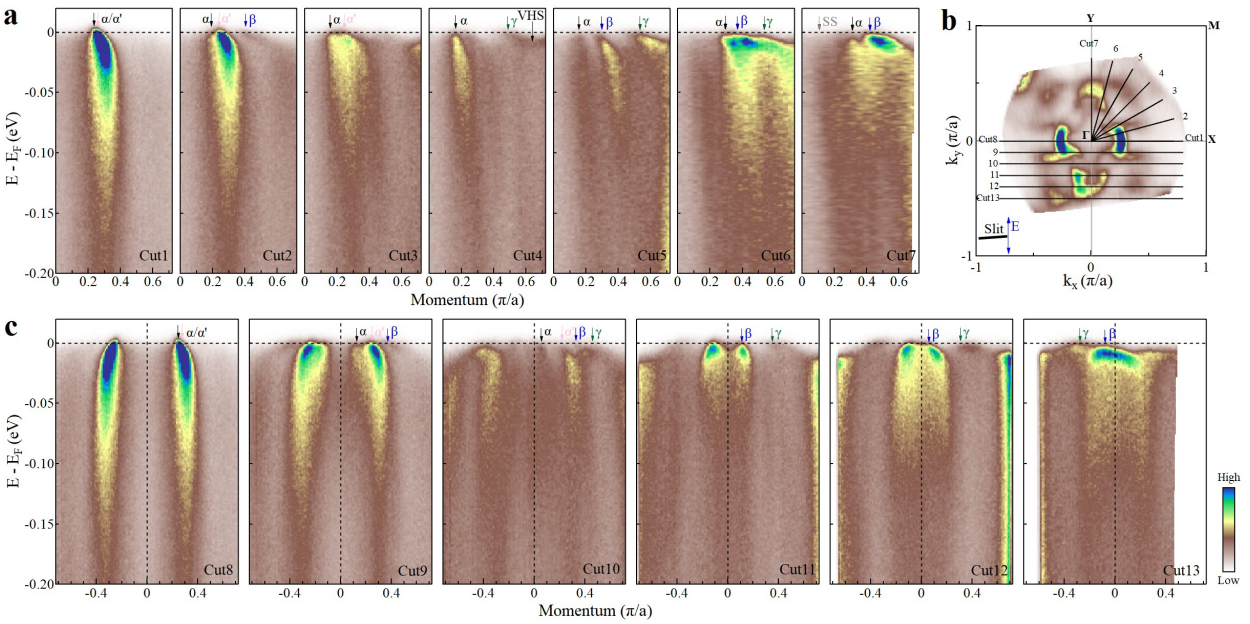


FIG. 3. **Detailed band structures of $CsFe_2As_2$ measured 18 K by laser ARPES. These are obtained from the same measurement shown in Fig. 1e.** **(a)**, Band structures along the momentum cuts Cut1-Cut7. These momentum cuts all cross the zone center and their locations are marked by black lines in **b**. The observed bands are labeled by the corresponding name of the Fermi surface as indicated in Fig. 1**j**. **(b)**, Fermi surface mapping of $CsFe_2As_2$ with the location of momentum cuts marked. **(c)**, Band structures along the momentum cuts Cut8-Cut13. These momentum cuts are parallel to Γ-X with their locations marked by black lines in **b**. The observed bands are also labeled by the corresponding name of the Fermi surface as indicated in Fig. 1**j**.

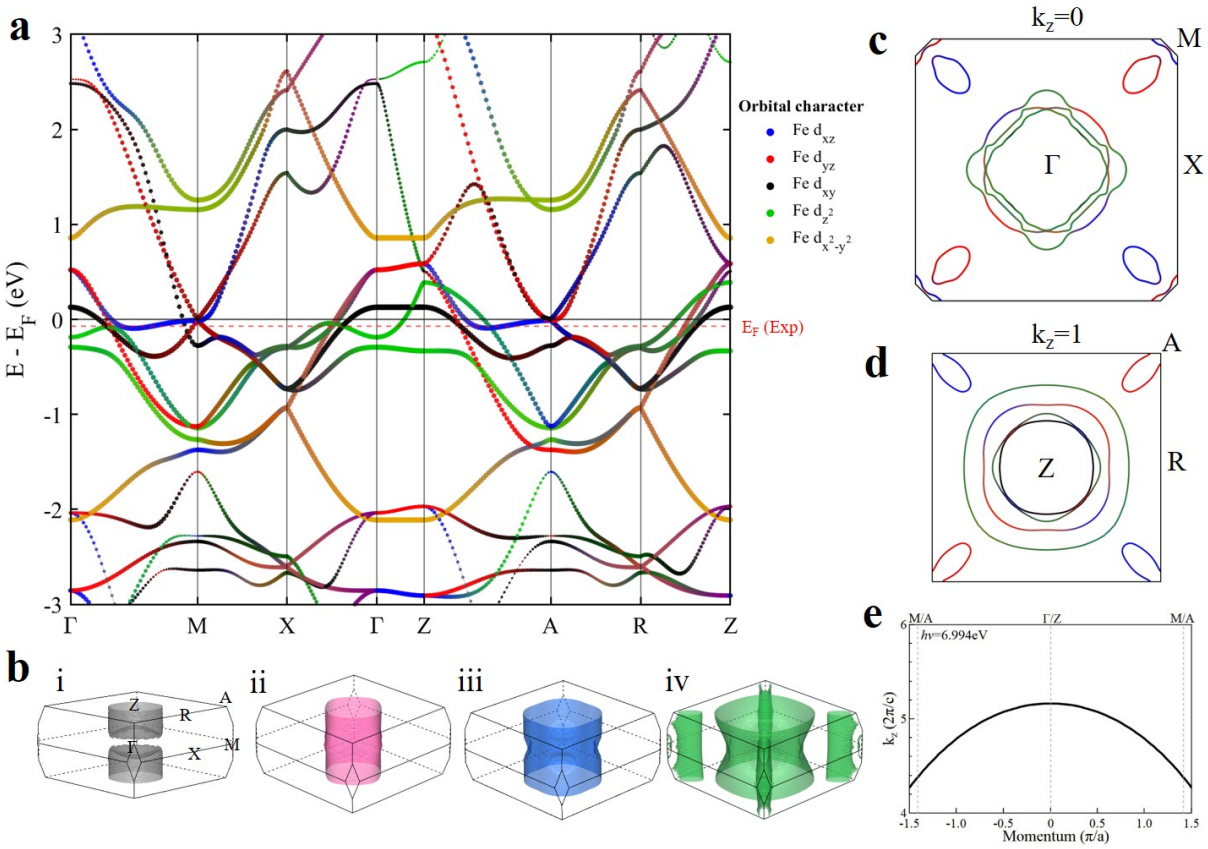


FIG. 4. **Calculated electronic structures of** $CsFe_2As_2$**. (a)**, Calculated band structure of $CsFe_2As_2$ along the high-symmetry momentum path Γ-M-X-Γ ($k_z = 0$) and Z-A-R-Z ($k_z = 1$), with the bands color-coded according to the Fe 3d orbital characters. The red dashed line indicates the experimental Fermi level (E_F(Exp)), located at $E_F - 0.07$ eV relative to the calculated Fermi level. **(b)**, Three-dimensional Fermi surface sheets calculated at the experimental Fermi level E_F(Exp). **(c,d)**, Corresponding constant-k_z Fermi surface contours at $k_z = 0$ and $k_z = 1$, respectively. **(e)**, Calculated relationship between the out-of-plane momentum k_z and the in-plane momentum $k_{\|}$ for the 6.994-eV laser-ARPES based on the free-electron final-state approximation, with an inner potential of $V_0 = 12$ eV determined from the photon-energy-dependent synchrotron ARPES measurements[23].

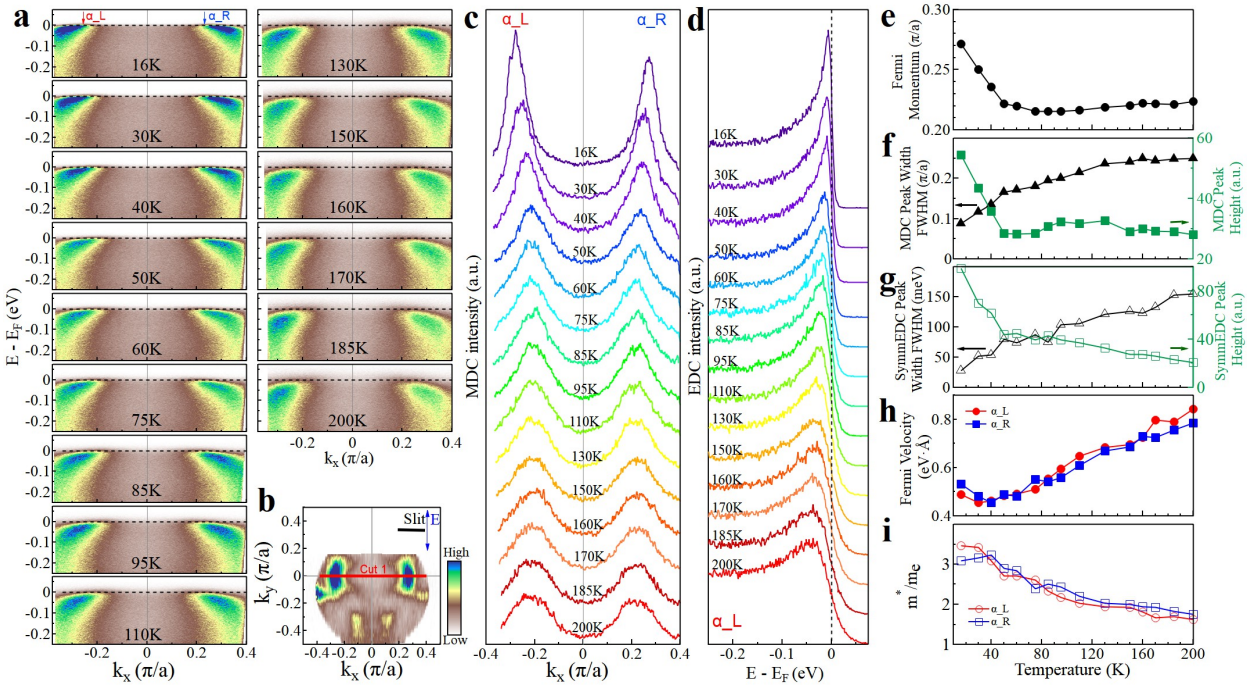


FIG. 5. **Temperature evolution of the hole-like α band in $CsFe_2As_2$ measured by laser ARPES. (a)**, Band structures of the α band measured along Γ-X at different temperatures. The location of the momentum cut (Cut1) is marked by the red line in **b**. The red and blue arrows in top-left panel indicate the Fermi momenta α_L (left band) and α_R (right band) of the observed α band. **(b)**, Fermi surface mapping of $CsFe_2As_2$ with the location of the momentum cut Cut1 marked. **(c)**, Momentum distribution curves (MDCs) at the Fermi level measured at different temperatures extracted from **a**. For clarity, these curves are offset vertically along intensity scale. **(d)**, Energy distribution curves (EDCs) at the Fermi momentum α_L measured at different temperatures extracted from **a**. For clarity, these curves are also offset vertically along intensity scale. **(e)**, Temperature dependence of the Fermi momentum of the α band k_F^{α}. It is obtained by fitting the MDCs in **c** with two Lorentzians and averaging over the two extracted Fermi momenta ($k_F^{\alpha_\mathrm{L}}$ and $k_F^{\alpha_\mathrm{R}}$). **(f)**, Temperature dependence of the MDC peak width (full width at half maximum, FWHM) (black solid triangles, left scale) and MDC peak height (green solid squares, right scale) extracted also from fitting the MDCs in **c** with two Lorentzians and averaging over the values obtained from the left and right α bands. **(g)**, Temperature dependence of the symmetrized EDC peak width (FWHM) (black empty triangles, left scale) and symmetrized EDC peak height (green empty squares, right scale). The symmetrized EDCs are obtained from EDCs in **d** and then fitted with one Lorentzian to extract the width and height of symmetrized EDCs. **(h)**, Temperature dependence of the Fermi velocity of the α band. It is obtained by MDC fitting of the α bands in **a** and getting the slope of the dispersion near the Fermi level. The Fermi velocity extracted from the left α band (red solid circles) and the right α band (blue solid squares) is identical. **(i)**, Temperature dependence of the corresponding effective mass of the α band. It is obtained from the Fermi momentum (**e**) and the Fermi velocity (**h**) by the relation $m^* = \hbar k_F / v_F$. The effective mass obtained from the left α band (red empty circles) and the right α band (blue empty squares) is identical.

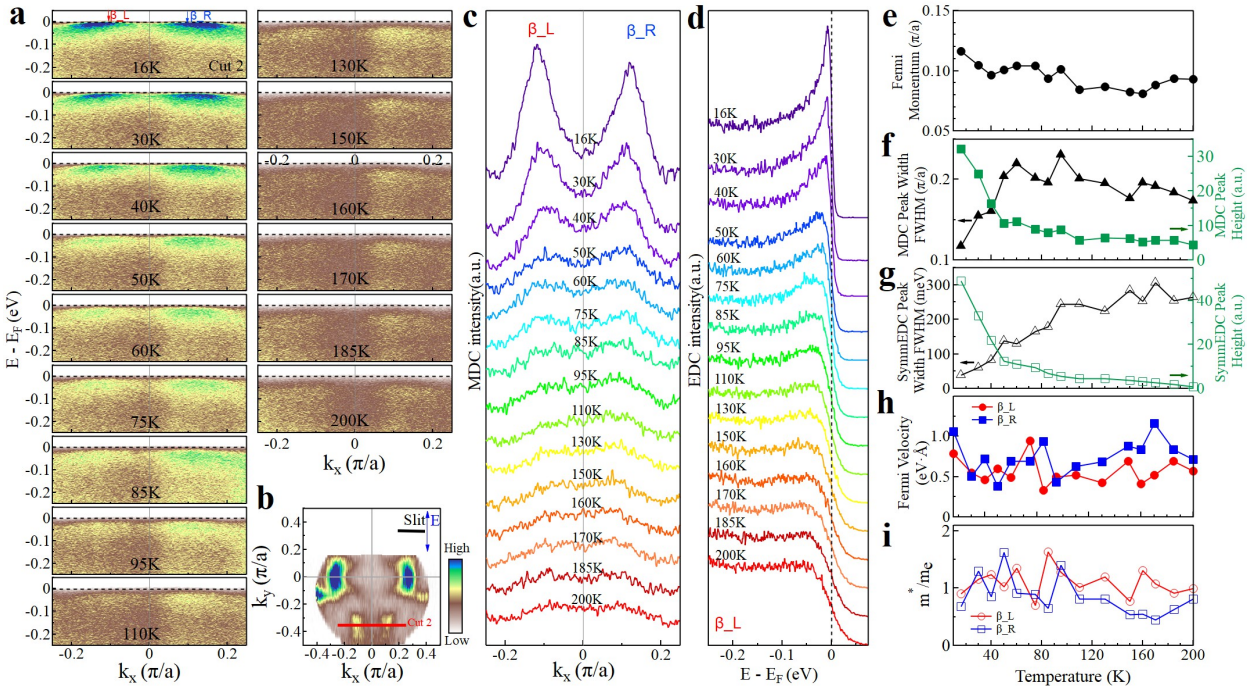


FIG. 6. **Temperature evolution of the hole-like β band in $CsFe_2As_2$ measured by laser ARPES. (a)**, Band structures of the β band measured along the momentum cut Cut2 at different temperatures. The location of the momentum cut (Cut2) is marked by the red line in **b**. The red and blue arrows in top-left panel indicate the Fermi momenta β_L (left band) and β_R (right band) of the observed β band. **(b)**, Fermi surface mapping of $CsFe_2As_2$ with the location of the momentum cut Cut2 marked. **(c)**, MDCs at the Fermi level measured at different temperatures extracted from **a**. For clarity, these curves are offset vertically along intensity scale. **(d)**, EDCs at the Fermi momentum β_L measured at different temperatures extracted from **a**. For clarity, these curves are also offset vertically along intensity scale. **(e)**, Temperature dependence of the Fermi momentum of the β band k_F^{β}. It is obtained by fitting the MDCs in **c** with two Lorentzians and averaging over the two extracted Fermi momenta ($k_F^{\beta_\mathrm{L}}$ and $k_F^{\beta_\mathrm{R}}$). **(f)**, Temperature dependence of the MDC peak width (FWHM) (black solid triangles, left scale) and MDC peak height (green solid squares, right scale) extracted also from fitting the MDCs in **c** with two Lorentzians and averaging over the values obtained from the left and right β bands. **(g)**, Temperature dependence of the symmetrized EDC peak width (FWHM) (black empty triangles, left scale) and symmetrized EDC peak height (green empty squares, right scale). The symmetrized EDCs are obtained from EDCs in **d** and then fitted with one Lorentzian to extract the width and height of symmetrized EDCs. **(h)**, Temperature dependence of the Fermi velocity of the β band. It is obtained by MDC fitting of the β bands in **a** and getting the slope of the dispersion near the Fermi level. The Fermi velocity extracted from the left β band (red solid circles) and the right β band (blue solid squares) is similar. **(i)**, Temperature dependence of the corresponding effective mass of the β band. It is obtained from the Fermi momentum (**e**) and the Fermi velocity (**h**) by the relation $m^* = \hbar k_F / v_F$. The effective mass obtained from the left β band (red empty circles) and the right β band (blue empty squares) is similar.